REPORT

High rectification and gate-tunable photoresponse in 1D-2D lateral van der waals heterojunctions

Pu Wang,[1,2,3,4] Haoran Mu,[1,4,*] Tinghe Yun,[1,4] Depeng Ji,[1,4] Bohan Wei,[1] Zengxia Mei,[1] Lede Xian,[1] Qingqing Ke,[2] Guangyu Zhang,[1] and Shenghuang Lin[1,*]
*Correspondence: muhaoran@sslab.org.cn (H.M.); linshenghuang@sslab.org.cn (S.L.)
Received: September 11, 2024; Accepted: December 16, 2024; Published Online: December 23, 2024; https://doi.org/10.59717/j.xinn-mater.2024.100113

GRAPHICAL ABSTRACT

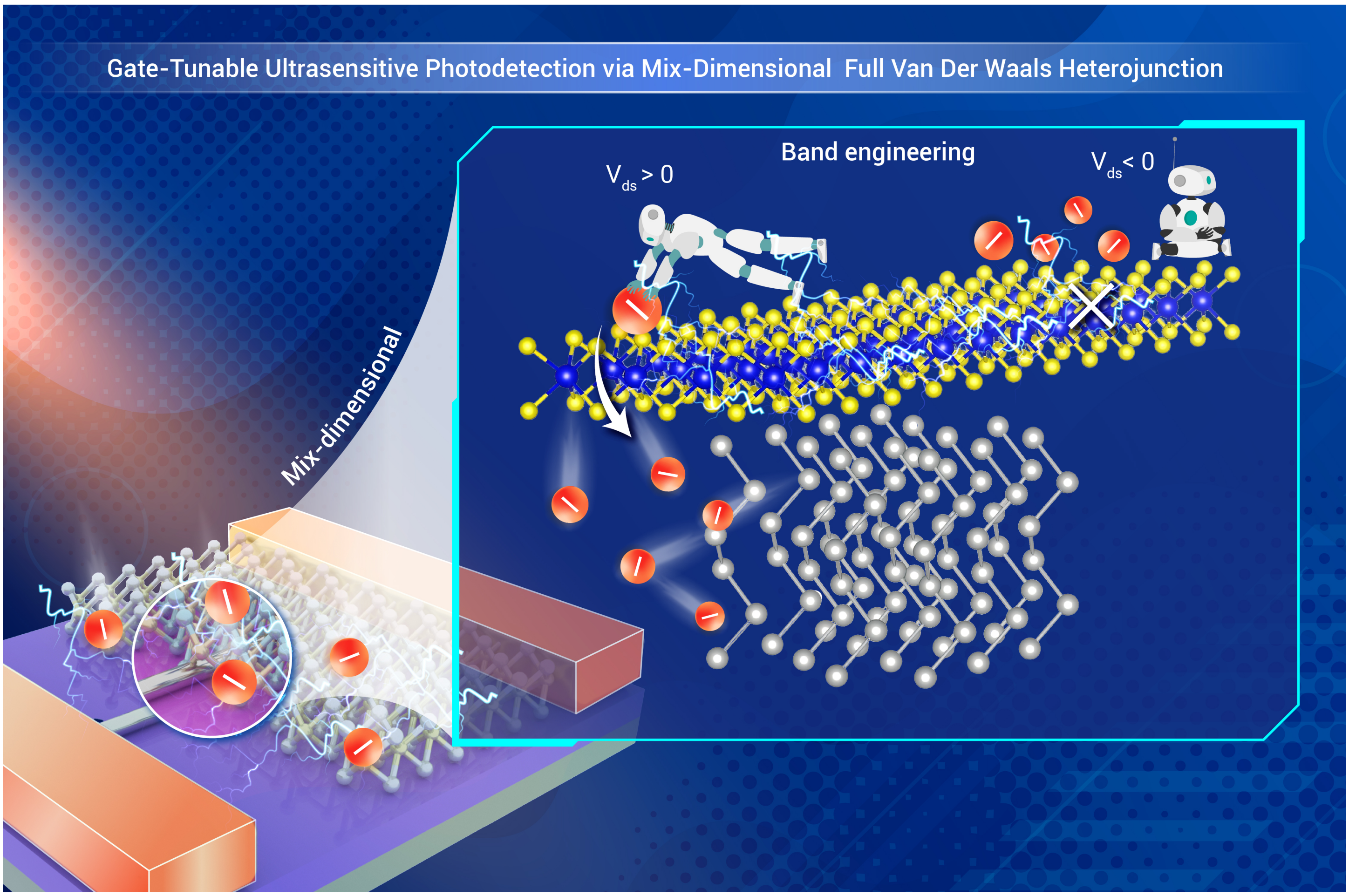

PUBLIC SUMMARY

- Fully van der Waals-integrated (vdWs) gate-tunable photodiode based on 1D Te–2D WS_2 heterojunction.
- Achieves both a high rectification ratio and on/off ratio simultaneously, with ultra-low dark current.
- High detectivity enables ultra-weak light detection, along with fast response time and excellent linearity.
- New insights into vdWs optoelectronics through band engineering, dimensional control, and interface design.

High rectification and gate-tunable photoresponse in 1D-2D lateral van der waals heterojunctions

Pu Wang,[1,2,3,4] Haoran Mu,[1,4,*] Tinghe Yun,[1,4] Depeng Ji,[1,4] Bohan Wei,[1] Zengxia Mei,[1] Lede Xian,[1] Qingqing Ke,[2] Guangyu Zhang,[1] and Shenghuang Lin[1,*]
[1]Songshan Lake Materials Laboratory, Dongguan 523808, China
[2]Guangdong Provincial Key Laboratory of Optoelectronic Information Processing Chips and Systems, School of Microelectronics Science and Technology, Sun Yat-sen University, Zhuhai 519082, China
[3]Institute of Semiconductors Henan Academy of Sciences, Zhengzhou 450000, China
[4]These authors contributed equally
*Correspondence: muhaoran@sslab.org.cn (H.M.); linshenghuang@sslab.org.cn (S.L.)

Received: September 11, 2024; Accepted: December 16, 2024; Published Online: December 23, 2024; https://doi.org/10.59717/j.xinn-mater.2024.100113

Citation: Wang P., Mu H., Yun T., et al. (2025). High rectification and gate-tunable photoresponse in 1D-2D lateral van der waals heterojunctions. *The Innovation Materials* **3**:100113.

The self-passivating surfaces and reduced tunneling leakage current enable the creation of ideal Schottky contacts in van der Waals (vdW) semiconductor heterojunctions. However, simultaneously achieving high rectification ratios, low reverse leakage currents, and rapid photoresponse remains challenging. Here, we present a one-dimensional (1D)/two-dimensional (2D) mixed-dimensional heterostructure photodiode to address these challenges. The significant valence band offset and minimal electron affinity difference in this structure ensure high rectification ratios and efficient charge collection. Additionally, the dimensional disparity between the 1D and 2D materials, characterized by a smaller contact area and significant thickness difference, results in low reverse leakage current and a high current on-off ratio. Moreover, it enables gate-tunable band structure transitions. Our device exhibits an exceptional rectifying ratio of 4.7×10^7 and a high on-off ratio of 5×10^7 (V_{ds} = 2 V and, V_g = 30 V) at room temperature. Under a gate voltage of 20 V, the photodiode achieves a specific detectivity (D^*) of 4.9×10^{14} Jones, a rapid response time of 14 μs, and an extended operational wavelength approaching to 1550 nm. The strategic combination of mixed-dimensional design and band engineering yields a 1D-2D p-n heterojunction photodiode with remarkable sensitivity, repeatability, and fast response, underscoring the potential of vdW semiconductors for advanced optoelectronic applications.

INTRODUCTION

Photodiodes, owing to their crucial light-sensitive and rectifying properties, have long been essential components in optoelectronics.[1-4] These diodes are conventionally based on p-n or p-i-n structures, demonstrating a high I_{light}/I_{dark} ratio operated under both reverse-biased and unbiased conditions. Recent advancements in this field have sparked significant interest in two-dimensional (2D) van der Waals (vdW) heterostructures.[5-7] These structures boast exceptional properties and high flexibility in assembly and integration, overcoming the constraints of lattice mismatch and impractical fabrication processes associated with conventional heterojunctions.[8-10] The vdW-based photodiodes provide high rectification ratios, low dark current, and noise, thus achieving high signal-to-noise ratios.[8,11,12] Furthermore, their atomic-thin nature and electrostatic tunability of Fermi levels render excellent candidates for gate-tunable photodetectors with enhanced and reconfigurable performance.[13-15]

Previous research has shown that combining a high rectifying ratio and on-off ratio in 2D-based diodes can be achieved by assembling two 2D layers with a substantial bandgap offset. For instance, a vertical heterostructure based on BP and MoS_2 (bandgap offset: ~1.5 eV)[16] achieved a rectifying ratio of 1×10^6 and an on-off ratio of 1×10^7. However, these performance metrics rely heavily on the ultra-short carrier injection length characteristics in vertical heterostructures. In lateral configurations or with extended carrier injection lengths, rectifying ratios tend to be moderate. This is due to significant reverse tunneling current in the atomically thin p-n region of 2D vdWs heterostructures, which compromises rectifying ratios.[17-19] Tunneling diodes, like the $MoTe_2$-MoS_2 asymmetrical junction with a rectifying ratio of 3×10^7, boost reverse tunneling current while suppressing forward current, yielding high reverse-rectification.[20] However, this can impede the transport and recombination of photo-excited carriers, potentially reducing photocurrent and light responsivity.[21] Thus, further research is essential to enhance rectification, gate-tunability, and photo-response characteristics in vdWs-based photodiodes.

In this study, we present a vdWs photodiode that leverages a 1D-2D mixed heterostructure to address these challenges. Specifically, we integrate Te and WS_2 to form this heterostructure. Te is a 1D chain semiconductor with a p-doped narrow-bandgap (~0.3 eV) and a vdWs-bonded surface.[22-25] WS_2, on the other hand, is a 2D n-doped large-bandgap semiconductor (~2 eV in monolayer WS_2) known for its remarkable gate-tunability.[26,27] These distinct dimensional properties, combined with the large offset in the valence band maximum and the full vdW combination, effectively suppress reverse tunneling and surface leakage currents while facilitating efficient charge separation, transport, and collection.[16,19] The structural feature ensures the simultaneous achievement of both a high current rectification ratio (4.7×10^7) and a high on-off ratio (5×10^7) at ambient temperature (~300 K) in the lateral heterojunction configuration. Furthermore, the minimal electron affinity difference (~0.08 eV) enhances the device's high light sensitivity under conventional charge-carrier transport conditions.[28] This small difference also allows for band alignment modulation through gate voltage application, increasing the device's performance flexibility and broadening its working wavelength range.

The heterojunction photodiode device demonstrates capability in photovoltaic and photoconductive detection operations. When a gate voltage of 20 V is applied, the photodiode exhibits a detectivity of up to 4.9×10^{14} Jones, coupled with a high I_{Light}/I_{dark} ratio of approximately 10^7, a rapid response of 14 μs, and an extended response range to 1550 nm. The dimensional disparity in the heterojunction region causes the WS_2 layer to be fully depleted, enhancing the generation and separation of photogenerated carriers, while the minimal electron affinity difference ensures efficient transport and collection of these carriers. These results highlight the superior capabilities of the 1D-2D heterojunction photodiode, providing valuable insights into the design and engineering of high-performance vdWs devices for advanced optoelectronic applications.

MATERIALS AND METHODS

Material synthesis and device fabrication

Te nanowires (NWs) were synthesized with a modified solution-growth method.[22] Specifically, the precursor Na_2TeO_3 and polyvinylpyrrolidone (PVP, K30) were dissolved in deionized water with the added ammonia (NH_4OH, 25-28%, wt/wt%) and hydrazine hydrate (N_2H_4, 80%, wt/wt%) to adjust the pH to a value of ~10. This mixture was stirred magnetically until a homogeneous solution was obtained. Subsequently, the solution was sealed in a Teflon-lined stainless autoclave, heated to 180°C for a duration of 12 hours before allowing it to cool down to room temperature naturally. The resulting Te NWs can be obtained through centrifuging the solution at 7000 rpm for 5 min, followed by washing with deionized water and anhydrous ethanol for 3 times to remove the remaining impurity. The length and diameter of Te NWs can be controlled by manipulating the reaction time and the ratio of precursors.

To fabricate the Te/WS_2 heterojunction photodetector, the as-prepared Te NWs were dispersed on a SiO_2 (280 nm)/Si (p++) wafer surface by a spin-coating method. WS_2 flakes were prepared by exfoliating from the bulk crystals (sourced from HQ Graphene) with the conventional mechanical exfolia-

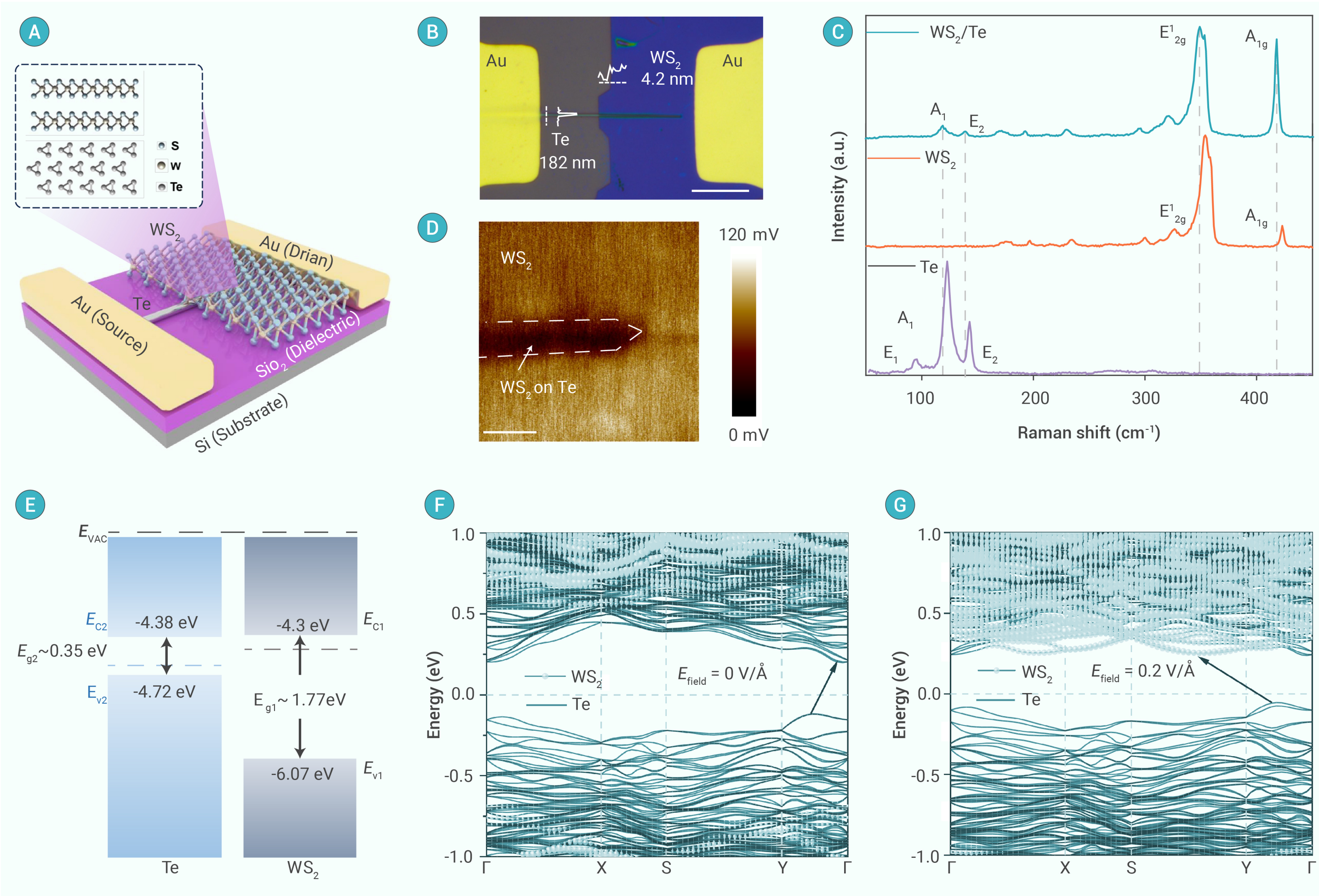

Figure 1. Schematic and characterization of the vdWs photodiode (A) Schematic illustration of the device architecture, showing the integration of Te (1D chain semiconductor) and WS_2 (2D layered semiconductor) with Au electrodes on a SiO_2/Si substrate. Inset: Atomic structures of Te and WS_2, demonstrating their crystallographic arrangement. (B) Optical image of the fabricated device, highlighting the dimensions of the Te (182 nm thickness) and WS_2 (4.2 nm thickness) layers. (C) Raman spectra of the Te/WS_2 heterostructure, WS_2, and Te, indicating characteristic peaks. (D) KPFM mapping of the Te-WS_2 heterojunction region. (E) Energy band alignment of Te and WS_2, showing the valence and conduction band positions. (F)-(G) Band structure of the heterojunction and the estimated band configuration of WS_2 in relation to the total band. (F) Band structure of WS_2 without an electric field (E_{field} = 0 V/Å). (G) Band structure of WS_2 with an applied electric field (E_{field} = 0.2 V/Å), demonstrating the modulation of electronic properties under external influence.

tion method.[2] The Te/WS_2 vdW heterojunction can be obtained by transferring the WS_2 nanoflakes onto the Te NW using a deterministic dry transfer method. Finally, drain/source electrodes were transferred on each side of the heterojunction with the assistance of Polypropylene carbonate (PPC, see more details in the reference).

Characterization and device measurements

The morphologies of tellurium nanowires were investigated by scanning electron microscope (SEM, Gemini 300, Zeiss). Aberration-corrected transmission electron microscopy microscope operating at 300 kV (AC-TEM Spectra 300 (S), Thermo Scientific), was used to characterize the crystal structure and the band structure of Te NWs. The thickness and topography of Te and WS_2 were determined by atomic force microscopy (AFM, Oxford, Cypher S). The Kelvin probe force microscopy (KPFM, Oxford, Cypher S) was performed to measure the surface potential of both WS_2 and Te. The Raman spectra and PL signals were collected by exciting the sample with a continuous wave 532 nm laser source (Horiba LabRam HR Evolution).

The electronic properties were measured using a commercial semiconductor parameter analyzer (Keysight, B1500) in a probe station (Lake Shore). The optoelectronic measurements were performed using the probe station equipped with an illumination source. The incident light signals were modulated by a generator (DG822, RIGOL, 25 MHz), and the output signal was recorded by an oscilloscope (PicoScope, pico Technology). The noise spectral density was measured using a spectrum analyzer (PDA, Fs-Pro). All these measurements were carried out under ambient conditions without special treatments.

First-principles calculations

The calculations are implemented in the Vienna Ab-initio Simulation Package within density functional theory.[29,30] The projector augmented wave potentials and the generalized gradient approximation with the Perdew-Burke-Ernzerhof (PBE) exchange-correlation functional are used.[31,32] The DFT-D2 vdW corrections are used to handle the van der Waals interactions of the 2D materials. Spin-orbit coupling was considered in the self-consistent DFT calculations. For the structural optimization of Te, an energy cutoff of 600 eV and 21×21×21 Monkhorst-Pack scheme k-points sampling are used. For WS_2, an energy cutoff of 600 eV and 15×15×5 Monkhorst-Pack scheme k-points sampling are used. For the Te/WS_2 heterojunction slab, to simplify the calculations, an energy cutoff of 600 eV, 1×1×1 k-points sampling and 20 Å vacuum thickness are used and the lattice constants of the heterojunction supercell are fixed while the internal atomic positions are optimized until the residual force per atom is less than 0.01 eV/Å.

RESULTS

Device architecture and energy band determination

To construct the lateral heterojunction, we placed a few-layer WS_2 flake on top of a Te nanowire. The structural quality of the solution-grown Te nanowires was assessed using various techniques, including scanning elec-

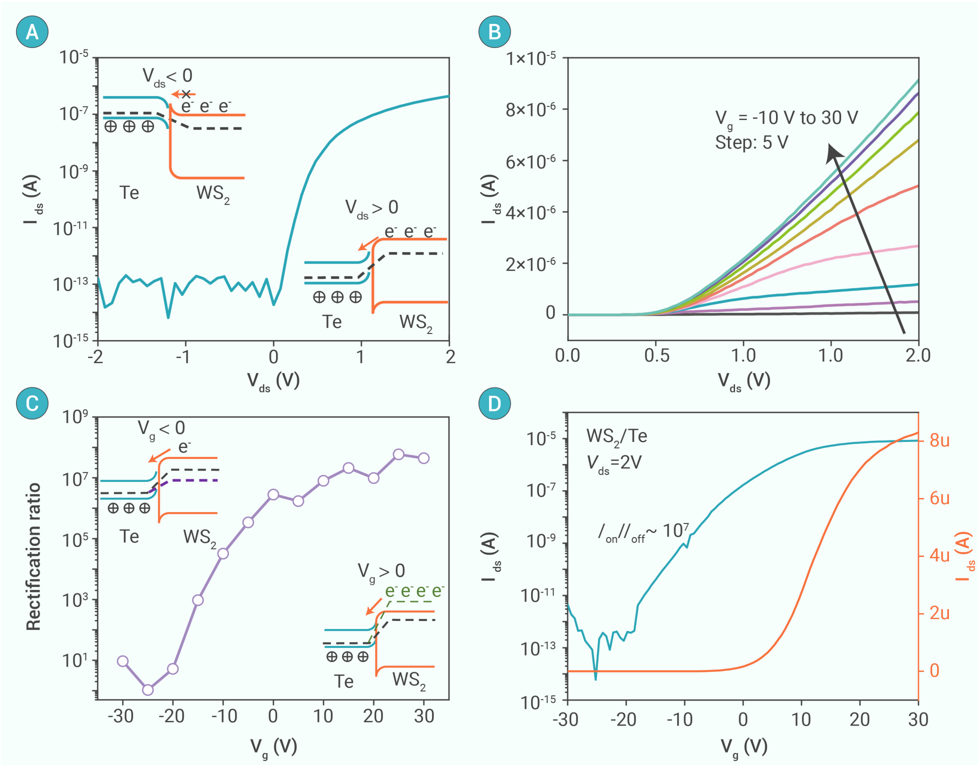

Figure 2. Electrical transport properties of the Te/WS_2 heterojunction device (A) Current-voltage (*I*-*V*) characteristics of the Te/WS_2 heterojunction at room temperature (~300 K), demonstrating typical diode behavior. The left inset shows the band alignment under reverse-bias conditions, while the right inset illustrates the band alignment under forward-bias conditions. The gate voltage V_g is 0 V. (B) Output curves of the heterojunction with varying back-gate voltages from -10 V to 30 V. (C) Rectification ratio as a function of V_g with the voltage range of V_{ds} from -2 V to 2V. The inset shows the detailed rectification behavior under varying gate voltages, highlighting the impressive gate-tunability and high on-off ratio of the device. (D) The I_{ds}-V_g transfer characteristics at a V_{ds} of 2 V at 300 K, indicating "n-type" behavior.

tron microscopy (SEM), energy-dispersive X-ray spectroscopy (EDS), spherical aberration-corrected scanning transmission electron microscopy (AC-STEM), and high-resolution transmission electron microscopy (HRTEM). As shown in Figure S1, these analyses revealed an orderly alignment along the <0001> direction with no significant defects or dislocations. The thicknesses of the Te and WS_2 layers were confirmed to be 182 nm and 4.2 nm, respectively, through atomic force microscopy (AFM) results (Figure S2). The device was built on a SiO_2/Si substrate with a 300 nm thick SiO_2 dielectric layer. To minimize the Fermi pinning effect at the metal-semiconductor interface, we used a novel electrode transfer technique, as detailed in the Methods section (Figure S3).

Figure 1A shows a schematic diagram of the fully van der Waals-configured 1D-2D heterojunction FET device, with an optical micrograph in Figure 1B. The naturally formed van der Waals interactions between Te and WS_2 are depicted in the inset of Figure 1A. SEM imaging at the overlapping region confirmed a solid interface without air bubbles, and EDS analysis at the same location revealed the precise chemical composition of the Te/WS_2 heterojunction (Figure S4). Subsequent Raman spectroscopy measurements demonstrate pronounced raman shifts of Te and WS_2 peaks, further affirming the well-constructed Te/WS_2 heterojunction (Figure 1C).

In addition to the AFM measurement to determine the thicknesses of Te and WS_2 layers, KPFM mapping was also performed for studying the surface potential of the heterojunction. Interestingly, as shown in Figure 1D, the measured surface potential of WS_2 in the overlapping area significantly differs from that in other regions, decreasing by approximately 100 mV. This indicates that the WS_2 in the overlapping area is fully charge-depleted.[19,33] Using a diffusion-emission model, the depletion region width was calculated to be approximately 44.3 nm, providing further evidence for this observation (see more details in Supplementary Note 1).[34-37]

We then investigated the energy band alignment of the Te/WS_2 heterojunction using comprehensive characterization techniques, including photoluminescence (PL, Figure S5), ultraviolet photoelectron spectroscopy (UPS, Figure S6), electron energy loss spectroscopy (EELS, Figure S7), and Kelvin probe force (KPFM, Figure S8). The conduction band minimum (CBM), valence band maximum (VBM), and Fermi level for both Te and WS_2 are determined, as illustrated in Figure 1E and detailed in Figure S9. The experimental results indicate that Te is p-type while WS_2 is n-type, with a substantial valence band offset exceeding 1.2 eV. This significant offset creates a potential well conducive to carrier reservation, suggesting a high rectifying ratio for the heterojunction. The Fermi level difference between the materials is approximately 0.13 eV, indicating a modest barrier spike in the conduction band. The near-zero electron affinity difference (~0.07 eV) suggests that the energy band type can be effectively transitioned.

To further understand the electronic properties, we performed density functional theory (DFT) simulations, which corroborated the experimental findings. The DFT calculations revealed a type-I energy band alignment under equilibrium conditions, where both the CBM and VBM are predominantly influenced by the Te nanowire (Figure 1F). When an external electric field of 0.2 V/Å was applied for gate modulation, the energy band alignment transitioned from type-I (straddling) to type-II (staggered) (Figure 1G, more details in Notes S2-S3 & Figure S10). This transition alters the interlayer carrier transport mechanisms, presenting opportunities for gate-driven functionalities in the FET device.

Electrical behavior

Leveraging mixed-dimensional and band alignment engineering in van der Waals heterojunctions based on Te and WS_2, our device demonstrates excellent carrier transport performance. The current-voltage (*I*-*V*) characteristics of the Te/WS_2 heterojunction at room temperature (~300 K) are illustrated in Figure 2A, revealing prototypical diode behavior. Under thermal equilibrium conditions (0 V bias), a potential barrier is established, which intensifies under reverse-bias conditions, thereby restricting the predominant carrier drift current (left inset, Figure 2A). When a forward-bias voltage is applied to the p-n junction, the potential barrier across the junction decreases, causing an exponential increase in current with applied voltage (right inset, Figure 2A). The ultralow reverse leakage current is measured to be less than 10^{-13} A at -2 V bias, yielding an exceptional rectifying ratio of 5×10^6. This low reverse current significantly enhances photodetector performance by improving the signal-to-noise ratio, dynamic range, and specific detectivity.

The gate-modulation capabilities of the heterojunction are presented in the output and transfer curves in Figures 2B & D. As the back-gate voltage increases from -10 V to 30 V, electrostatic doping modulates the density of free electrons and holes in the junction, leading to an increased rectification ratio. An exceptional rectification ratio of 4.7×10^7 is achieved with a 30 V gate voltage (Figures 2B & S11C), the highest reported for van der Waals heterojunctions with lateral configurations to our knowledge. Figure 2D shows the I_{ds}-V_g transfer characteristics at a V_{ds} of 2 V at 300 K, revealing a monotonically "n-type" behavior. The on-off ratio is highly pronounced at ~ 5×10^7, achieved simultaneously with the impressive rectifying behavior.

The rectification ratio versus V_g is extracted to further demonstrate the gate-tunable capability of the p-n heterojunction field-effect transistor, as illustrated in Figure 2C. The source-drain current under negative bias remains minimal, while the current under positive bias increases significantly, leading to a rising rectification ratio. Since Te is insensitive to gate modulation due to its thickness in the hundreds, the drain current is predominantly influenced by

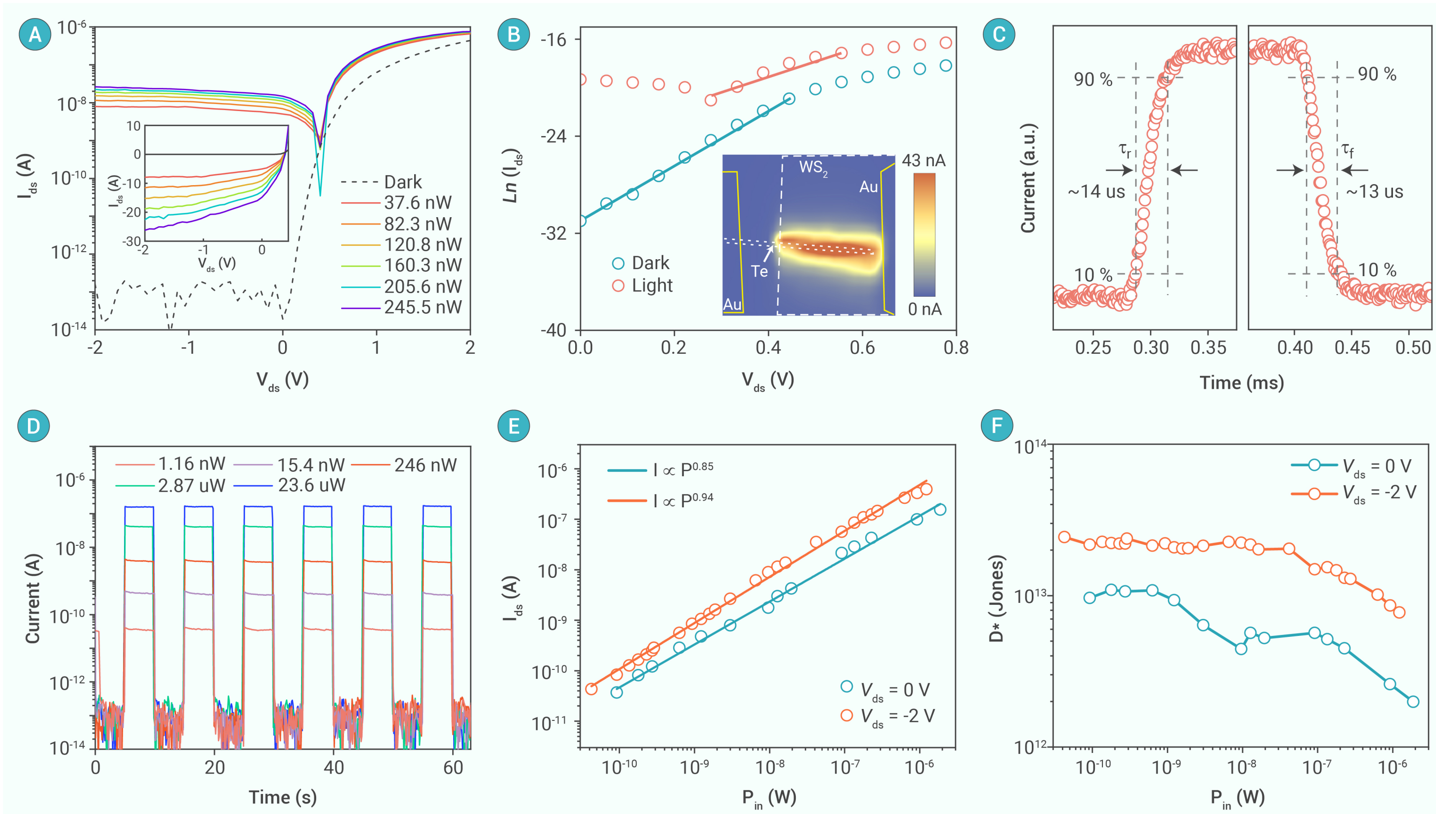

Figure 3. Optoelectronic response of the Te/WS_2 photodiode device without gate modulation (A) I_{ds} - V_{ds} curves under zero gate voltage in the dark and with different light intensities at room temperature (~300 K), illustrating the device's photodiode behavior. Inset: linear I_{ds} - V_{ds} curves from -2 V to 0.45 V, showing the detailed behavior in the photoconductive and photovoltaic regions. (B) ln (I_{ds}) - V_{ds} plots of the Te/WS_2 device under dark and 638 nm light conditions. The ideality factor is 1.4 in the dark and 2.73 under illumination, respectively. Inset: Photocurrent mapping data, confirming the photocurrent generation is localized at the heterojunction. (C) Temporal response of the device under 638 nm laser illumination. (D) Photo-switching response under different light intensities, indicating high stability and repeatability in its photodetection capabilities. The I_{light}-I_{dark} ratio is over 10^6. (E) Photocurrent as a function of laser power densities, showing the θ of the power law up to 0.85 and 0.94 at V_{ds} = 0 V and -2 V, respectively. (F) Calculated detectivity (D^*) under varying light intensities, highlighting the device's sensitivity.

the n-type WS_2 channel. Under negative V_g, the electron population diminishes, resulting in low current. The rectification ratio decreases to only ~1.05 at -25 V of V_g. Conversely, under positive V_g, the accumulated electrons in the WS_2 flake contribute to a rectification ratio exceeding 7 orders of magnitude (inset, Figure 2C).

The mechanisms behind the gate-tunable rectification and ultralow reverse current are elucidated. For a fully depleted heterojunction, as shown in the KPFM result in Figure S8, and with negligible surface current impeded by the electron barrier of the heterojunction, the theoretical approximation for the reverse leaky current (IR) is expressed as[38]:

$$I_R = \frac{qn_iW}{\tau_g}A$$

where n_i denotes the intrinsic carrier concentration, A represents the junction area, W signifies the junction thickness, and τ_g is the carrier generation lifetime. The 1D nature of the Te nanowire plays a crucial role in diminishing the junction area of the mixed-dimensional heterostructure, which is notably smaller than that of previously reported 2D-2D heterostructures, resulting in a reduction of I_R. Furthermore, the implementation of a fully van der Waals configuration significantly diminishes tunneling leaky current.[8] The substantial valence band offset further decelerates minor carrier diffusion, thereby contributing to the observed diminishment of I_R.[16] The reduced-dimensional nature of the heterostructure also ensures high gate-tunability and an impressive on-off ratio, further enhancing device performance (more details in Figure S12).

An Arrhenius analysis of the dark current further explains the suppression of reverse leaky current in the heterostructure (Figure S13).[39] The black solid line represents experimental data, while dashed lines represent fitted dark-current components, including total current, diffusion current, trap-assisted tunneling (TAT) current, band-to-band (BTB) current, and generation-recombination (G-R) current.[40-42] It is evident that tunneling current components are effectively suppressed to undetectable levels. The ideal factor (n), denoting the proportion between G-R and diffusion current, is determined to be ~1.4, revealing that the diffusion current is the predominant component.[43] This value is significantly smaller than that observed in conventional heterojunction p-n diodes (where n >> 2), indicating low G-R current and charge trap density in the Te/WS_2 heterojunction.

Optoelectronic response without gate modulation

Here, we focus on the photoresponse of the Te-WS_2 heterojunction devices. Figure 3A presents the I_{ds} - V_{ds} curves without gate voltage under both dark conditions and 638 nm laser irradiation with intensities ranging from 37.6 to 245.5 nW, with the photocurrent exceeding 0.7 μA at +2 V bias (Figure S14A). However, under forward bias, despite the exponential increase in current with the applied voltage, the depletion region narrows, leading to increased dark current and reduced light detectivity. Consequently, the key operational focus is on the negative and zero bias regions. The linear I_{ds} - V_{ds} plots at negative and small bias voltages are enlarged in the inset of Figure 3A. Under negative voltages, the device operates in the photoconductive region, where the photocurrent is generated by the separation of photogenerated electron-hole pairs. Since the reverse leakage current remains negligible, this region shows good linearity and a high signal-to-noise ratio. At zero bias, the device exhibits photovoltaic behavior, generating an open-circuit voltage due to the built-in electric field at the heterojunction. A short-circuit current (I_{sc} = 14.8 nA) and open-circuit voltage (V_{oc} = 0.4 V) can be observed under the power of 245.5 nW, resulting in effective photoelectric conversion capability of the device. The output electrical power P_{el}, defined as P_{el} = I_{ds}·V_{ds}, describes the electricity generation capability of a photodiode and is shown in Figures S14A-C.

The underlying illumination-driven current mechanism is investigated. The

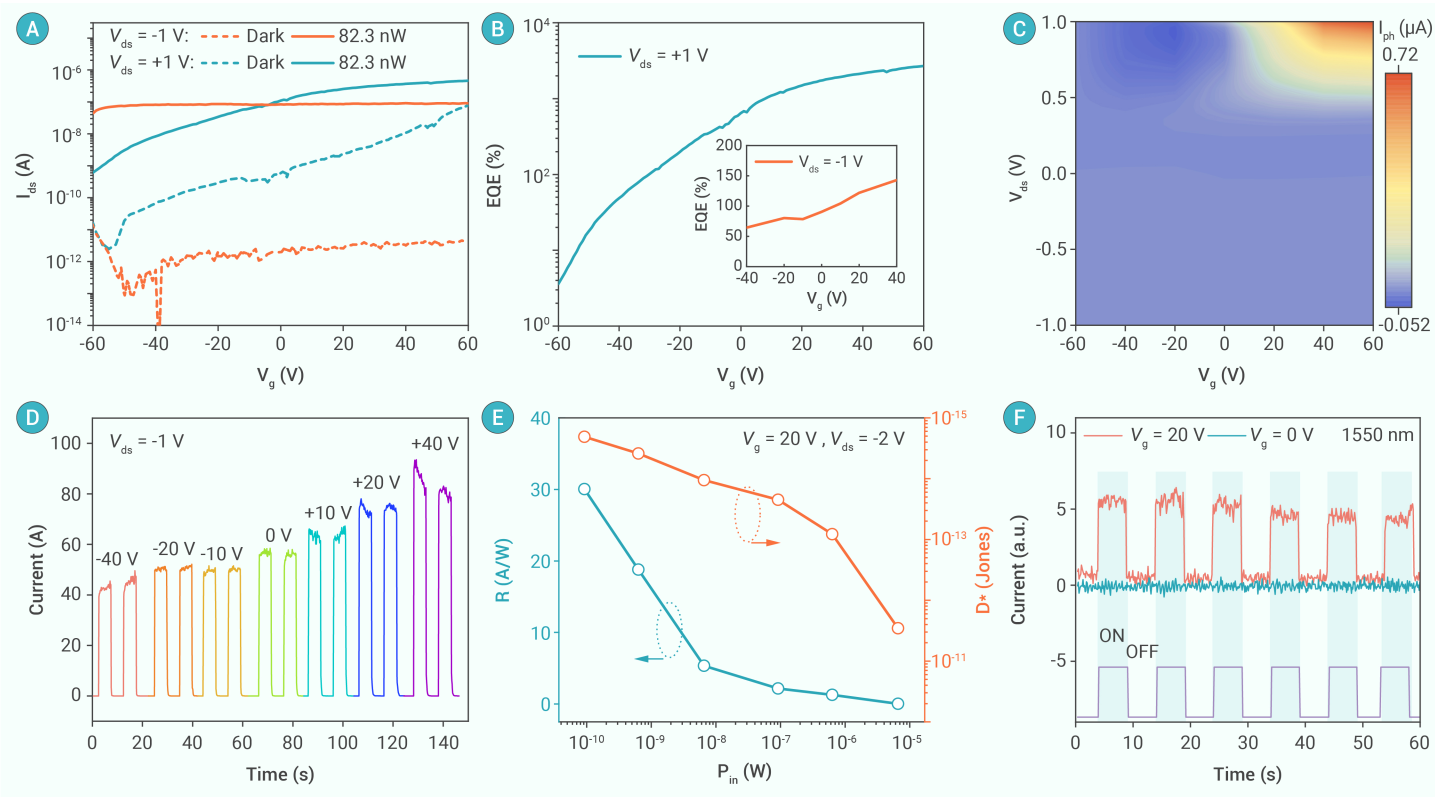

Figure 4. Gate-modulated photoresponse characteristics of Te/WS_2 heterojunction photodiodes (A) I_{ds}-V_g curves of the device under dark (dotted lines) and illuminated (solid lines) states. V_{ds} was set to ± 1 V. (B) *EQE* as a function of back-gate voltage at a positive bias voltage (+1 V) under 638 nm laser excitation. Inset: *EQE* of the device at a negative bias voltage (-1 V). (C) Photocurrent (I_{ph}) at 638 nm illumination as a function of the gate (V_g) and source-drain (V_{ds}) biases. When applying both positive V_g and V_{ds}, the photogating effect leads to the remarkable photocurrent. (D) Photo-switching response of the Te/ WS_2 heterojunction device under different gate voltages from -40 V to 40 V. (E) Power-dependent responsivity (R) and detectivity (D^*) values of the Te/ WS_2 heterojunction photodiode under 638 nm laser illumination at V_{ds} = -2 V, V_g = 20 V. (F) Near-infrared (1550 nm) response of the Te/ WS_2 heterojunction photodiode with (red line) and without (blue line) gate voltages.

ideality factor, reflecting the balance between generation-recombination (G-R) and diffusion current, increases from ~1.4 in the dark to ~2.73 under 638 nm light irradiation (Figure 3B, the details are in Figure S15). This increase implies a significant rise in G-R current within the depletion region, suggesting the crucial role of the heterojunction in photocarrier generation and separation. Figure S16 provides further insights through tunneling current analysis. The replotted ln (I_d/V^2) − V^{-1} curve indicates that at negative and low positive bias voltages, direct tunneling (DT) processes dominate, facilitated by the "spike" barrier at the conduction band of Te and WS_2. This efficient separation of photoinduced charge carriers is beneficial for achieving high performance and indicates that the high energy band offset and barrier significantly impede the dark current but do not adversely affect the photocurrent. At higher positive bias, the electric field enables electrons to tunnel through the energy barrier, leading to Fowler-Nordheim tunneling (FNT) dominance.

The optoelectrical mechanisms are further revealed through the combination of current analysis and spatially resolved photocurrent mapping, as shown in Figure S17. At zero and negative voltages, the photocurrent is dominated by the drift of minority carriers, and the photogenerated carriers are rapidly separated by the depletion region of the heterojunction and transmitted to the corresponding electrodes, resulting in a sensitive optoelectronic response (the inset of Figure 3B). At positive voltages higher than the open-circuit voltage, the drift of the minority carriers is suppressed, and the device current is dominated by majority carrier diffusion, with photocurrent generation shifting to the WS_2-metal junction area (Figure S17D & G).

Beyond the impressive photocurrent, the Te-WS_2 photodiode exhibits a remarkably fast response speed. Figure 3C shows the temporal response at 0 V bias voltage, with a rise time of approximately 14 μs and a fall time of around 13 μs. The high-quality heterojunction interface between Te and WS_2 facilitates efficient charge separation and minimizes recombination losses, while the 1D-2D device design results in low capacitance, enabling quick charge collection and release. In addition to the inherently high mobility of Te and exfoliated WS_2, photogenerated charges are collected and released rapidly, leading to the fast rise and fall times observed in the device's photovoltaic mode.

Then we investigated the photo-switching performance and sensitivity of the Te-WS_2 photodiode. In Figure 3D, under zero bias conditions, the device exhibits rapid and stable on/off switching between light and dark states. A maximum photocurrent of 0.1 μA, along with the dark current of 0.13 pA, a high photo-to-dark current ratio I_{on}/I_{off} is achieved to ~ 10^6. More details are provided in Figure S18A. Applying a -2 V bias between the source and drain significantly increases the photocurrent while limiting the dark current to sub-pA levels, reaching the detectable limit of comparable 1D-2D heterojunctions (Figure S18B).[44-46] On the other hand, at a positive bias, due to the increased majority carrier diffusion and reduced electric field across the junction, the rapid collection of photogenerated carriers, the I-T response significantly slows down (Figure S18C). The relationship between photocurrent and laser power density under zero (photovoltaic mode) and negative bias (photoconductive mode) voltages is illustrated in Figure 3E. Following the power law, $I_{ph} = AP^{\theta}$, the device demonstrates a near-linear relationship with θ values of approximately 0.85 at 0 V and 0.94 at -2 V. The negative bias enhances the electric field across the heterojunction, facilitating efficient separation and rapid transport of photogenerated electron-hole pairs, thereby improving linearity.

To quantitatively evaluate the performance of the 1D-2D heterojunction photodiode, we calculated the responsivity (R), external quantum efficiency (EQE), and specific detectivity ($D*$) from the I-T curves. The EQE, which measures the number of charge carriers generated per incident photon, is plotted against the incident power (P_{in}) in Figure S19A. Due to the efficient separation of photogenerated carriers in the high-quality heterojunction, the EQE reaches nearly 100% under 638 nm illumination without an external electric field. In the photoconductive mode at -2 V bias, the peak EQE exceeds 200%, showcasing the device's superior charge collection capabilities. Correspondingly, the responsivity reaches approximately 1.0 A/W (Figure S19B). The specific detectivity ($D*$) highlights the photodiode's sensitivity to detect

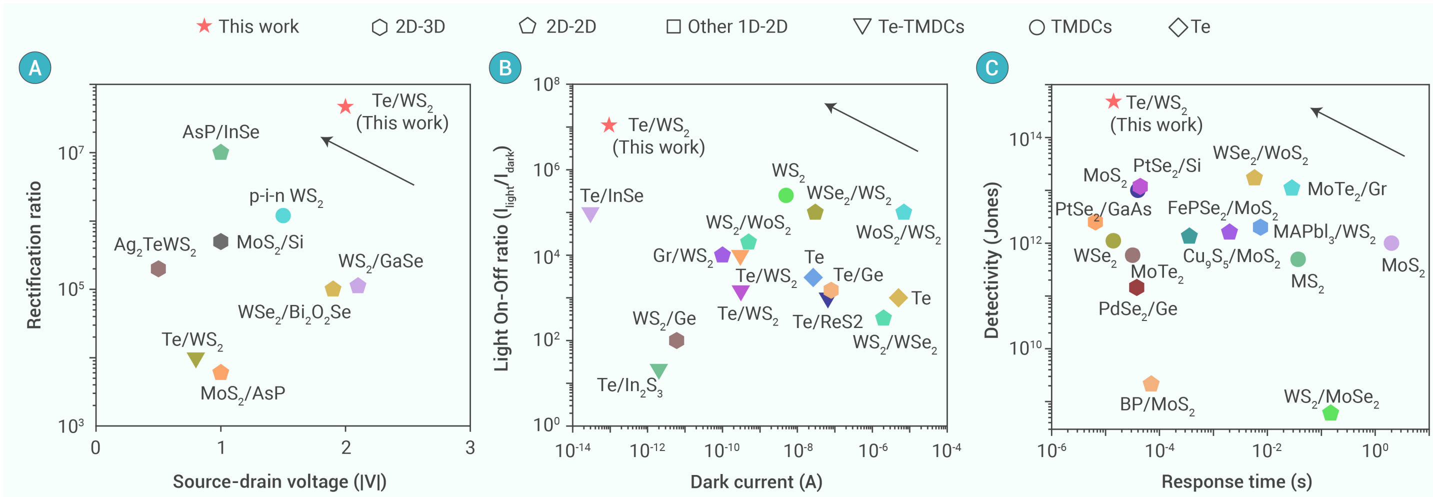

Figure 5. Benchmarking the performance of the Te/WS_2 heterojunction photodiode against other 2D material-based photodetectors (A) Comparison of reverse rectification ratios at various biases ($|V_{ds}|$) among state-of-the-art 2D vdW devices. The Te/WS_2 photodiode exhibits a superior rectification ratio of 4.7×10^7 at $|V_{ds}| = 2$ V, outperforming many recent 2D devices (Supplementary Table 1). (B) Comparison of dark current and light on-off ratio (I_{light}/I_{dark}) at room temperature for different 2D photodetectors. The Te/ WS_2 photodiode demonstrates an ultralow dark current and high I_{light}/I_{dark} ratio, highlighting its enhanced performance (Supplementary Table 2). (C) Specific detectivity (D^*) versus response speed (τ_f) for various 2D and mixed-dimensional photodetectors. The Te/WS_2 photodiode achieves higher D^* values while maintaining a fast response speed, indicating a well-balanced performance between detectivity and response time (Supplementary Table 3). The comparison includes Te, TMDCs, Te-TMDCs (WS_2, MoS_2, and so on), other 1D-2D, 2D-2D, and 2D-3D heterostructures, with the Te/WS_2 photodiode demonstrating outstanding performance among these categories.

low-intensity light with minimal noise. With its high responsivity and exceptionally low dark noise current, the $D*$ values consistently remain above 10^{13} Jones for a wide range of light intensities under both 0 V and -2 V biases, with a peak detectivity of around 3.6×10^{13} Jones at -2 V bias (Figure 3F).

Gate-modulated photoresponse characteristics

To investigate the gate-modulated photoresponse of the Te/WS_2 p-n heterojunction field-effect transistor, we examined the I_{ds}-V_g transfer curves under 638 nm illumination, as shown in Figure 4A. Compared to the transfer curves in the dark (dashed lines in Figure 4A), significant photoresponses are observed in both negative and positive bias modes (-1 V and +1 V V_{ds}). Under positive bias, trapped carriers more effectively modulate the channel conductance, allowing the photogating effect to dominate. This results in a substantial change in the photocurrent with varying gate voltages, leading to an increase in *EQE* from ~ 3.6% to ~ 2692% at +1 V V_{ds} (Figure 4A). In contrast, under negative bias, the strong built-in electric field primarily drives carrier separation. Although photogating still occurs, its relative contribution to the overall photocurrent is less significant compared to the intrinsic electric field effects. As the gate voltage varies from -60 V to 60 V, the *EQE* at -1 V V_{ds} increases from ~ 64.4% to ~ 142% (inset of Figure 4A).

Figure 4C plots the photocurrent (the difference of I_{ds} under dark and illumination, I_{ph}) as a function of gate (V_g) and source-drain (V_{ds}) voltages. The corresponding output curves under different gate voltages in dark and 638 nm illumination conditions are provided in Figure S20. Under illumination, the gate voltage effectively controls the number of trapped carriers, modulating the overall photocurrent, further demonstrating the role of photogating in enhancing the device's photoresponse. When both positive V_g and V_{ds} are applied, the accumulation of photo-excited carriers in the channel significantly enhances the device's conductance, leading to a remarkable increase in photocurrent up to 0.7 μA.

The photo-switching behavior is critical for a photodetector. Figure 4D illustrates the performance of the Te/WS_2 heterojunction device under different gate voltages. With gate modulation, the current switching between light and dark states remains rapid and stable in the negative bias region. As the gate voltage increases to +40 V, the on-state photocurrent rises by over 1.58 times compared to that at zero gate voltage. The *I*-*T* curves under varying illumination intensities exhibit good repeatability and stability (Figure S21). At a power intensity of 7.92 μW, the device achieves a maximum photocurrent of 0.37 μA and a high I_{light}/I_{dark} of ~ 10^7.

The performance metrics of the photodetector under negative bias (-2 V) and a +20 V gate voltage (V_g) are thoroughly evaluated. The linearity of the photodetector, characterized by the fitted power exponent θ, decreases to approximately 0.67 with the 20 V gate voltage (Figure S22A). This reduction in linearity is attributed to the photogating effect, which introduces nonlinearity by trapping and releasing carriers, thereby modulating the photocurrent response more strongly at higher light intensities. Figure 4E demonstrates that with a 20 V gate voltage, the maximum responsivity (*R*) increases to approximately 30 A/W, and the corresponding detectivity ($D*$) reaches around 4.9×10^{14} Jones. This significant enhancement is due to the photogating effect, which greatly improves the device's sensitivity. Figures S22B-D further compares the *EQE*, *R*, and $D*$ with and without the 20 V gate voltage, while the dark noise currents under different bias and gate conditions are provided in Figure S23. These figures of merit, which are crucial for measuring the sensitivity of the photodetector, improve by over 12 times under negative bias with gate modulation.

In addition to enhanced sensitivity, the operational wavelength range of the photodetector is broadened by applying gate voltages. Effective modulation of the gate voltage relative to the Fermi energy level shifts the energy band alignment at the heterojunction interface from type-I to type-II (Figures 1D-E & S10). This transition enhances the interlayer transport properties of carriers and enables the development of high-performance gate-driven optoelectronic devices. The near-infrared (1550 nm) response of the Te/WS_2 heterojunction photodiode with and without gate voltage is shown in Figure 4F. At V_g = 0 V, the large valence band offset in the Te/WS_2 vdW heterojunction blocks the photogenerated holes, resulting in no response under 1550 nm light (blue line in Figure 4F). However, under V_g = 20 V, the spike barrier in the conduction band is reduced, allowing photogenerated electrons in the narrow-bandgap Te to be effectively excited and transported to the conduction band of WS_2, enabling a significant photoresponse (red line in Figure 4F).

Benchmark of device performances

To benchmark our 1D-2D Te/WS_2 heterojunction photodiode, we compared its performance with other state-of-the-art 2D material-based photodetectors, including those based on Te, TMDCs, Te-TMDCs (WS_2), other 1D-2D, 2D-2D, and 2D-3D heterojunctions. The rectification ratio of our Te/WS_2 photodiode is exceptionally high, reaching 4.7×10^7 at a small bias of $|V_{ds}| = 2$ V (Figure 5A & Table S1). This surpasses that of vertically structured van der Waals heterojunctions, such as BP/MoS_2,[13] and the reverse rectification ratios of tunneling-based heterojunctions like AsP/InSe.[47] Additionally, the high current on/off ratio from the transfer curves demonstrates the effectiveness of gate modulation and the evolution of energy band alignment in our device.

The optoelectronic response characteristics of our device were then evaluated. Due to the efficient rectification effect, the photodiode exhibits a significantly low dark current and a high I_{light}/I_{dark} ratio compared to other 2D-based photodetectors (Figure 5B & Table S2). Gate voltage modulation further enhances the photodiode's specific detectivity ($D*$). Figure 5C shows that our device achieves higher $D*$ values while maintaining a fast response speed, placing it among the best-performing photodetectors in the comparison (Table S3). This balanced performance between detectivity and response time is attributed to the unipolar potential barrier all-van der Waals heterojunction design, which facilitates both ultra-weak light detection and ultrafast response.

The high sensitivity, fast response speed, and excellent repeatability of our Te/WS_2 photodiode make it suitable for practical applications such as ultra-weak light image sensing. To demonstrate this, we implemented a single-pixel confocal scanning imaging system with a 405 nm light source for imaging measurements, as illustrated in the schematic diagram in Figure S24A. An image with a high spatial resolution of 635 × 485 pixels was obtained, capturing intensity information at different positions of the logo pattern. Additionally, an image with a resolution of 800 × 350 pixels clearly displaying the "SLAB" lettering confirms the device's high stability (Figure S24A). The integration time for each pixel was only 0.5 ms, thanks to the photodetector's fast response. Furthermore, due to the device's high detectivity, stable photocurrent measurements were achievable even when the light power was as low as 12.8 pW (Figure S24C-D). These results underline the potential of our Te/WS_2 photodiode for high-resolution, low-light imaging applications, showcasing its capability to operate effectively in ultra-weak light conditions with rapid and reliable performance.

CONCLUSIONS

We have demonstrated a 1D-2D mixed-dimensional heterostructure photodiode based on Te nanowires and WS_2. This unique material combination leverages a significant valence band offset and minimal electron affinity difference, enabling efficient charge collection and high rectification ratios. The device exhibits an exceptional rectifying ratio of 4.7×10^7 and a high on-off ratio of 5×10^7 at room temperature. The dimensional disparity between the 1D and 2D materials, characterized by a smaller contact area and significant thickness difference, results in low reverse leakage current, a high current on-off ratio, and gate-tunable band structure transitions. Under a gate voltage of 20 V, the photodiode achieves a specific detectivity ($D*$) of 4.9×10^{14} Jones, a rapid response time of 14 μs, and an extended operational wavelength range up to 1550 nm. These results mark a significant advancement in the field of optoelectronics, presenting a promising solution for applications requiring high sensitivity, stability, and rapid response.

REFERENCES

1. Michel J., Liu J. and Kimerling L. C. (2010). High-performance Ge-on-Si photodetectors. *Nat. Photonics* **4**:527–534. DOI:10.1038/nphoton.2010.157
2. Lee J., Georgitzikis E., Hermans Y., et al. (2023). Thin-film image sensors with a pinned photodiode structure. *Nat. Electron.* **6**:590–598. DOI:10.1038/s41928-023-01016-9
3. Lischke S., Peczek A., Morgan J. S., et al. (2021). Ultra-fast germanium photodiode with 3-dB bandwidth of 265 GHz. *Nat. Photonics* **15**:925–931. DOI:10.1038/s41566-021-00893-w
4. Wang P., Lan Y., Huan C., et al. (2023). Recent progress on performance-enhancing strategies in flexible photodetectors: From structural engineering to flexible integration. *Mater. Sci. Eng. R Rep.* **156**:100759. DOI: 10.1016/j.mser.2023.100759
5. Geim A. K. and Grigorieva I. V. (2013). Van der Waals heterostructures. *Nature* **499**:419–425. DOI:10.1038/nature12385
6. Jariwala D., Marks T. J. and Hersam M. C. (2017). Mixed-dimensional van der Waals heterostructures. *Nat. Mater.* **16**:170–181. DOI:10.1038/nmat4703
7. Zhuang R., Cai S., Mei Z., et al. (2023). Solution-grown BiI/BiI_3 van der Waals heterostructures for sensitive X-ray detection. *Nat. Commun.* **14**:1621. DOI:10.1038/s41467-023-37297-z
8. Liu Y., Guo J., Zhu E., et al. (2018). Approaching the Schottky–Mott limit in van der Waals metal–semiconductor junctions. *Nature* **557**:696–700. DOI:10.1038/s41586-018-0129-8
9. Mu H., Zhuang R., Cui N., et al. (2023). Alternating BiI_3–BiI van der Waals photodetector with low dark current and high-performance photodetection. *ACS Nano* **17**:21317–21327. DOI:10.1021/acsnano.3c05849
10. Wang Y., Mei L., Li Y., et al. (2024). Integration of two-dimensional materials based photodetectors for on-chip applications. *Phys. Rep.* **1081**:1-46. DOI: https://doi.org/10.1016/j.physrep.2024.06.001
11. Zhang X., Liu B., Gao L., et al. (2021). Near-ideal van der Waals rectifiers based on all-two-dimensional Schottky junctions. *Nat. Commun.* **12**:1522. DOI:10.1038/s41467-021-21861-6
12. Wang G., Sun Y., Yang Z., et al. (2024). Near-ideal Schottky junction photodetectors based on semimetal-semiconductor van der Waals heterostructures. *Adv. Funct. Mater.* **34**:2316267. DOI: 10.1002/adfm.202316267.
13. LaGasse S. W., Dhakras P., Watanabe K., et al. (2019). Gate-tunable graphene–WSe_2 heterojunctions at the Schottky–Mott limit. *Adv. Mater.* **31**:1901392. DOI: 10.1002/adma.201901392
14. Huo N. and Konstantatos G. (2017). Ultrasensitive all-2D MoS_2 phototransistors enabled by an out-of-plane MoS_2 PN homojunction. *Nat. Commun.* **8**:572. DOI:10.1038/s41467-017-00722-1
15. Buscema M., Groenendijk D. J., Steele G. A., et al. (2014). Photovoltaic effect in few-layer black phosphorus PN junctions defined by local electrostatic gating. *Nat. Commun.* **5**:4651. DOI:10.1038/ncomms5651
16. Huang M., Li S., Zhang Z., et al. (2017). Multifunctional high-performance van der Waals heterostructures. *Nat. Nanotechnol.* **12**:1148–1154. DOI:10.1038/nnano.2017.208
17. Yu W. J., Li Z., Zhou H., et al. (2013). Vertically stacked multi-heterostructures of layered materials for logic transistors and complementary inverters. *Nat. Mater.* **12**:246–252. DOI:10.1038/nmat3518
18. Kang J., Jariwala D., Ryder C. R., et al. (2016). Probing out-of-plane charge transport in black phosphorus with graphene-contacted vertical field-effect transistors. *Nano Lett.* **16**:2580–2585. DOI:10.1021/acs.nanolett.6b00144
19. Wu F., Li Q., Wang P., et al. (2019). High efficiency and fast van der Waals hetero-photodiodes with a unilateral depletion region. *Nat. Commun.* **10**:4663. DOI:10.1038/s41467-019-12707-3
20. Cheng R., Wang F., Yin L., et al. (2018). High-performance, multifunctional devices based on asymmetric van der Waals heterostructures. *Nat. Electron.* **1**:356–361. DOI:10.1038/s41928-018-0086-0
21. Tan C., Yin S., Chen J., et al. (2021). Broken-gap PtS_2/WSe_2 van der Waals heterojunction with ultrahigh reverse rectification and fast photoresponse. *ACS Nano* **15**:8328–8337. DOI:10.1021/acsnano.0c09593
22. Wang Y., Qiu G., Wang R., et al. (2018). Field-effect transistors made from solution-grown two-dimensional tellurene. *Nat. Electron.* **1**:228–236. DOI:10.1038/s41928-018-0058-4
23. Qin J.-K., Liao P.-Y., Si M., et al. (2020). Raman response and transport properties of tellurium atomic chains encapsulated in nanotubes. *Nat. Electron.* **3**:141–147. DOI:10.1038/s41928-020-0365-4
24. Wu W., Qiu G., Wang Y., et al. (2018). Tellurene: its physical properties, scalable nanomanufacturing, and device applications. *Chem. Soc. Rev.* **47**:7203–7212. DOI:10.1039/C8CS00598B
25. Yu J., Mu H., Wang P., et al. (2024). Anisotropic van der Waals tellurene-based multifunctional, polarization-sensitive, in-line optical device. *ACS Nano* **18**:19099–19109. DOI:10.1021/acsnano.4c03973
26. Zhao W., Ghorannevis Z., Chu L., et al. (2013). Evolution of electronic structure in atomically thin sheets of WS_2 and WSe_2. *ACS Nano* **7**:791–797. DOI:10.1021/nn305275h
27. Hong X., Kim J., Shi S.-F., et al. (2014). Ultrafast charge transfer in atomically thin MoS_2/WS_2 heterostructures. *Nat. Nanotechnol.* **9**:682–686. DOI:10.1038/nnano.2014.167
28. Seib D. H. and Aukerman L. W. (1973). Photodetectors for the 0.1 to 1.0 μm spectral region. Marton L. and Marton C. (Eds). *Adv. Electron. Electron Phys.* (Academic Press) **34**, pp 95-221.
29. Went C. M., Wong J., Jahelka P. R., et al. (2019). A new metal transfer process for van der Waals contacts to vertical Schottky-junction transition metal dichalcogenide photovoltaics. *Sci. Adv.* **5**:eaax6061. DOI:10.1126/sciadv.aax6061
30. Kresse G. and Furthmüller J. (1996). Efficient iterative schemes for ab initio total-energy calculations using a plane-wave basis set. *Phys. Rev. B* **54**:11169–11186. DOI:10.1103/PhysRevB.54.11169
31. Kresse G. and Furthmüller J. (1996). Efficiency of ab-initio total energy calculations for metals and semiconductors using a plane-wave basis set. *Comput. Mater. Sci.* **6**:15-50. DOI: 10.1016/0927-0256(96)00008-0
32. Perdew J. P., Burke K. and Ernzerhof M. (1996). Generalized gradient approximation made simple. *Phys. Rev. Lett.* **77**:3865–3868. DOI:10.1103/PhysRevLett.77.3865
33. Wang F., Liu Z., Zhang T., et al. (2022). Fully depleted self-aligned heterosandwiched van der Waals photodetectors. *Adv. Mater.* **34**:2203283. DOI: 10.1002/adma.202203283
34. Garrity O., Rodriguez A., Mueller N. S., et al. (2022). Probing the local dielectric function of WS_2 on an Au substrate by near field optical microscopy operating in the visible spectral range. *Appl. Surf. Sci.* **574**:151672. DOI: 10.1016/j.apsusc.2021.151672
35. Sharma T., Thakur R. and Sharma R. (2021). Structural, electronic and dielectric properties of tellurium 1-D nanostructures : a DFT study. *Appl. Phys. A* **128**:41. DOI:10.1007/s00339-021-05183-4
36. Luo L.-B., Liang F.-X., Huang X.-L., et al. (2012). Tailoring the electrical properties of tellurium nanowires via surface charge transfer doping. *J. Nanopart. Res.* **14**:967. DOI:10.1007/s11051-012-0967-5

37. Rogalski A. (2022). Detectivities of WS_2/HfS_2 heterojunctions. *Nat. Nanotechnol.* **17**:217–219. DOI:10.1038/s41565-022-01076-6
38. Wu X., Kalliopuska J. and Eränen S., et al. (2012). Recent advances in processing and characterization of edgeless detectors. *J. Instrum* **7**:C02001. DOI:10.1088/1748-0221/7/02/C02001
39. Ren D., Meng X., Rong Z., et al. (2018). Uncooled photodetector at short-wavelength infrared using InAs nanowire photoabsorbers on InP with p–n heterojunctions. *Nano Lett.* **18**:7901–7908. DOI:10.1021/acs.nanolett.8b03775
40. Shockley W. (1949). The theory of p-n junctions in semiconductors and p-n junction transistors. *Bell Syst. Tech. J* **28**:435–489. DOI:10.1002/j.1538-7305.1949.tb03645.x
41. Sah C. t., Noyce R. N. and Shockley W. (1957). Carrier generation and recombination in P-N Junctions and P-N junction characteristics. *Proc. IRE* **45**:1228–1243. DOI:10.1109/JRPROC.1957.278528
42. Chen Y., Wang Y., Wang Z., et al. (2021). Unipolar barrier photodetectors based on van der Waals heterostructures. *Nat. Electron.* **4**:357–363. DOI:10.1038/s41928-021-00586-w
43. Williams K. J. and Esman R. D. (1999). Design considerations for high-current photodetectors. *J. Lightwave Technol.* **17**:1443–1454. DOI:10.1109/50.779167
44. Wang W., Wang W., Meng Y., et al. (2022). Mixed-dimensional anti-ambipolar phototransistors based on 1D GaAsSb/2D MoS_2 heterojunctions. *ACS Nano* **16**:1036–11048. DOI:10.1021/acsnano.2c03673
45. You J., Jin Z., Li Y., et al. (2024). Epitaxial growth of 1D Te/2D $MoSe_2$ mixed-dimensional heterostructures for high-efficient self-powered photodetector. *Adv. Funct. Mater.* **34**:2311134. DOI: 10.1002/adfm.202311134.
46. Tao J.-J., Jiang J., Zhao S.-N., et al. (2021). Fabrication of 1D Te/2D ReS_2 mixed-dimensional van der Waals p-n heterojunction for high-performance phototransistor. *ACS Nano* **15**:3241–3250. DOI:10.1021/acsnano.0c09912
47. Wu F., Xia H., Sun H., et al. (2019). AsP/InSe van der Waals tunneling heterojunctions with ultrahigh reverse rectification ratio and high photosensitivity. *Adv. Funct. Mater.* **29**:1900314. DOI: 10.1002/adfm.201900314

FUNDING AND ACKNOWLEDGMENTS

We acknowledge the support from the Guangdong Basic and Applied Basic Research Foundation (No. 2021B1515120034), National Key R&D Program of China (No. 2021YFA1202902), National Natural Science Foundation of China (No. 12204336 and No. 62204165), and Natural Science Foundation of Guangdong Province of China (2024A1515010350). The funders had no role in study design, data collection and analysis, decision to publish, or preparation of the manuscript.

AUTHOR CONTRIBUTIONS

P.W., H.M., T.Y., and D.J. contributed equally to this study. H.M., T.Y., and S.L. conceived and supervised the project. P.W. and B.W. performed most of the experiments and analyses. Z.M. assisted with the photographs of the samples and with the provision of instrumentation for the device preparations. D.J. and L.X. carried out computational simulations and analyzed the results. P.W., T.Y., H.M., Q.K, G.Z. and S.L. wrote and revised the manuscript. All authors commented on the submitted manuscript.

DECLARATION OF INTERESTS

The authors declare no competing interests.

DATA AND MATERIALS AVAILABILITY

All data supporting the findings of this study are available from the corresponding author upon reasonable request.

SUPPLEMENTAL INFORMATION

It can be found online at https://doi.org/10.59717/j.xinn-mater.2024.100113